Research progress and future prospects in the service security of key blast furnace equipment

Yanxiang Liu, Kexin Jiao, Jianliang Zhang, Cui Wang, Lei Zhang, and Xiaoyue Fan

View the article online at SpringerLink or IJMMM Webpage.

Articles you may be interested in

Hao-bin Zhu, Wen-long Zhan, Zhi-jun He, Ying-chang Yu, Qing-hai Pang, and Jun-hong Zhang, Pore structure evolution during the coke graphitization process in a blast furnace, *Int. J. Miner. Metall. Mater.*, 27(2020), No. 9, pp. 1226-1233. https://doi.org/10.1007/s12613-019-1927-1

Jun Zhao, Shao-fei Chen, Xiao-jie Liu, Xin Li, Hong-yang Li, and Qing Lyu, Outlier screening for ironmaking data on blast furnaces, *Int. J. Miner. Metall. Mater.*, 28(2021), No. 6, pp. 1001-1010. https://doi.org/10.1007/s12613-021-2301-7

Long-zhe Jin and Xiao-meng Niu, Micromorphology and safety properties of meager and meager-lean coal for blast furnace injection, *Int. J. Miner. Metall. Mater.*, 28(2021), No. 5, pp. 774-781. https://doi.org/10.1007/s12613-020-2104-2

Peng Liu, Li-bo Zhang, Bing-guo Liu, Guang-jun He, Jin-hui Peng, and Meng-yang Huang, Determination of dielectric properties of titanium carbide fabricated by microwave synthesis with Ti-bearing blast furnace slag, *Int. J. Miner. Metall. Mater.*, 28(2021), No. 1, pp. 88-97. https://doi.org/10.1007/s12613-020-1985-4

Min-min Sun, Jian-liang Zhang, Ke-jiang Li, Ke Guo, Zi-ming Wang, and Chun-he Jiang, Gasification kinetics of bulk coke in the $CO_2/CO/H_2/H_2O/N_2$ system simulating the atmosphere in the industrial blast furnace, *Int. J. Miner. Metall. Mater.*, 26(2019), No. 10, pp. 1247-1257. https://doi.org/10.1007/s12613-019-1846-1

Tian-yang Hu, Ti-chang Sun, Jue Kou, Chao Geng, and Yong-qiang Zhao, Effects and mechanisms of fluorite on the co-reduction of blast furnace dust and seaside titanomagnetite, *Int. J. Miner. Metall. Mater.*, 24(2017), No. 11, pp. 1201-1210. https://doi.org/10.1007/s12613-017-1512-4

IJMMM WeChat   QQ author group

Research progress and future prospects in the service security of key blast furnace equipment

Yanxiang Liu[1], *Kexin Jiao*[1,2],✉, *Jianliang Zhang*[1,2], *Cui Wang*[1], *Lei Zhang*[1,2], *and Xiaoyue Fan*[1]

1) School of Metallurgical and Ecological Engineering, University of Science and Technology Beijing, Beijing 100083, China
2) Research Institute of Macro-Safety Science, University of Science and Technology Beijing, Beijing 100083, China

Abstract: The safety and longevity of key blast furnace (BF) equipment determine the stable and low-carbon production of iron. This paper presents an analysis of the heat transfer characteristics of these components and the uneven distribution of cooling water in parallel pipes based on hydrodynamic principles, discusses the feasible methods for the improvement of BF cooling intensity, and reviews the preparation process, performance, and damage characteristics of three key equipment pieces: coolers, tuyeres, and hearth refractories. Furthemoere, to attain better control of these critical components under high-temperature working conditions, we propose the application of optimized technologies, such as BF operation and maintenance technology, self-repair technology, and full-lifecycle management technology. Finally, we propose further researches on safety assessments and predictions for key BF equipment under new operating conditions.

Keywords: blast furnace; equipment; service security; blast furnace campaign; self-repair

1. Current situation of blast furnace (BF) safety and longevity in ironmaking

In 2022, China's BF molten iron production reached 864 million tons, and it accounted for over 65.9% of the global BF molten iron production (about 1.3 billion tons) [1]. BFs are considered the largest single high-temperature and high-pressure reactors, and they play a pivotal role in resource and energy consumption during the iron- and steel-making process. The safety of BF is crucial for societal well-being and overall economic and social development. Consequently, this aspect has become an important requirement in modern BF development [2–4]. With the continuous advancement of large-scale BFs in China, the development of large BFs with extended campaign duration is urgently needed to facilitate low-carbon metallurgy. Among large-scale BFs used worldwide, which feature a capacity exceeding 4000 m³, Asia hosts 40 (25 in China), Europe has 6, and the Commonwealth of Independent States and North and South America each have 4 units [5]. Fig. 1(a) presents the index data, such as utilization coefficient, coal ratio, and fuel ratio, on large-scale Chinese BFs (with above 4000 m³ capacity). Notably, they exhibit relatively favorable technical indicators, which menas that China has achieved remarkable progress in key technologies, such as large-scale BF design systems, core equipment, process theory, and intelligent control. Considerable development has also been made in the longevity of BFs. The BF campaign on China Baowu Steel Group Corporation

Limited (Baosteel), Wuhan Iron and Steel (Group) Company (Wusteel), Shougang Group (Shousteel), and other enterprises has reached more than 15 years. The campaign on No. 3 BF in Baosteel has reached nearly 19 years, which sets a record for the BF campaign in China [6–7]. As shown in Fig. 1(b), the line is the fitting line of the corresponding data, and the slope of the line represents the utilization coefficient. Notably, the average utilization coefficients of Chinese BFs exceed those of other countries, which indicates the maintenance of safe operations under high-utilization conditions within the campaigns of Chinese BFs. Preliminary estimates suggest that the increased average lifespan of a BF from 10 to 15 years, which resulted in potential CO_2 emissions reduction of up to approximately 5.57 million tons under a level-4000+ BF configuration. Ironmaking technology is promoted with the progress made in BF safety and longevity technology.

More than 900 BFs are currently in service in China [8]. With the increase in smelting intensity, hundreds of BFs must undergo safety maintenance every year. Serious accidents, such as BF hearth burnout, cause heavy economic losses and casualties, which greatly hinder the development of BF safety and longevity [9–10]. A number of large-scale BFs necessitate repair due to damage to the cooling equipment. The safety and campaign of BFs mainly depend on the lower part of the shaft, belly, bosh, tuyere, and hearth bottom. Fig. 2 shows the key equipment in different areas. Realization of the safety and longevity of BFs involves ensuring the safety of key
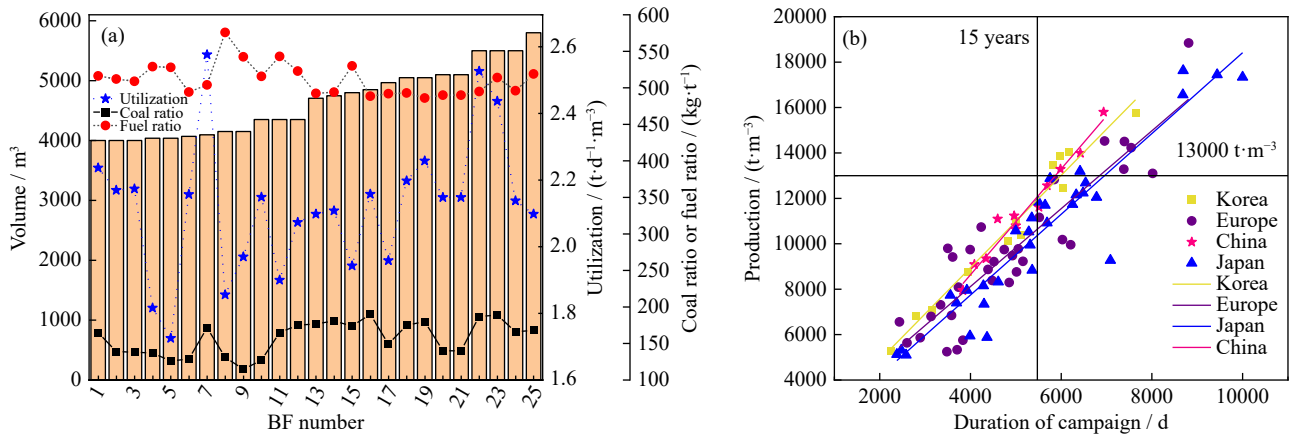
🌱 Springer

Fig. 1. Large-scale and longevity BF indexes: (a) the index data for prodution hot metal (HM) on 25 large-scale Chinese BFs; (b) the life and HM production of BFs in different countries.
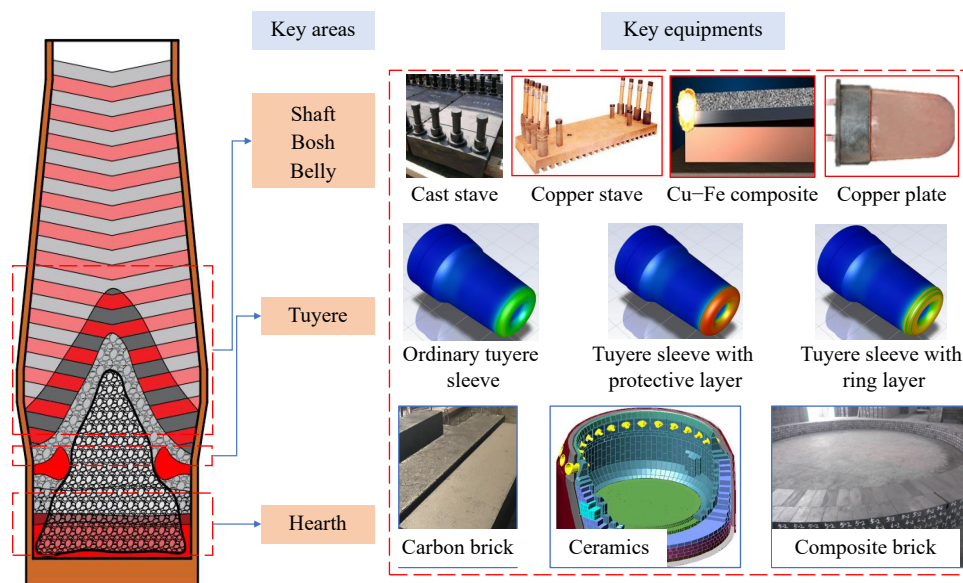

Fig. 2. Key equipments of BF for safety and longevity [11].

equipment in key areas during the long-term BF smelting process.

2. Basic principle of heat transfer in BF

2.1. Heat transfer characteristics

With the application of heat and mass transfer theory in BF cooling, considerable advancements have been attained in BF cooling technology. Notable variations have been observed in the temperature field distribution and the heat flux of the furnace at different BF heights under various operating conditions. Fig. 3(a) illustrates the temperature distribution trend of BFs. The primary effect of the cooling system lies in ensuring the safety and campaign longevity of BFs. Water in the cooling system removes the heat generated within the furnace [12–13]. The establishment of a reasonable temperature gradient helps in maintaining low temperatures for the BF lining while creating a protective layer on its hot sidewall surface. Fig. 3(b) demonstrates the distribution within the hearth's heat transfer system for BFs [10]. The

thermal resistance of molten iron and the protective layer on the hot surface of the refractory accounts for 30% of the total thermal resistance of the system, and the thermal resistance of the cooling system accounts for 3.3%. The internal condition of the BF hearth exhibits a far greater influence potential on heat transfer than the cooling system. Consequently, the direct contact between high-temperature gas, slag iron, and refractory materials is hindered, which reduces the erosion rates for refractory materials [14–15]; as a result, the long life of BF is realized.

2.2. Uniformity of water distribution

Measurements conducted on several BFs' cooling systems indicate uneven water supply volumes, which result in nonuniform circumferential water-supply distribution [16–18]. Circumferential water supply unevenness refers to the ratio of the difference between the maximum and minimum water velocities to the average water velocity in circumferential cooling water pipes. To quantify the unevenness within a BF's cooling system, numerical simulation methods were

A—molten iron; B—boundary layer; C—viscous layer; D—solid layer; α_1—combined heat transfer coefficient of cooling system, W/(m²·K); α_2—convective heat transfer coefficient of molten iron, W/(m²·K); L_1, L_2, and L_3—thickness of ram, refractory, and protective layer, m; λ_1, λ_2, and λ_3—thermal conductivity of ram, refractory, and protective layer, W/(m²·K).
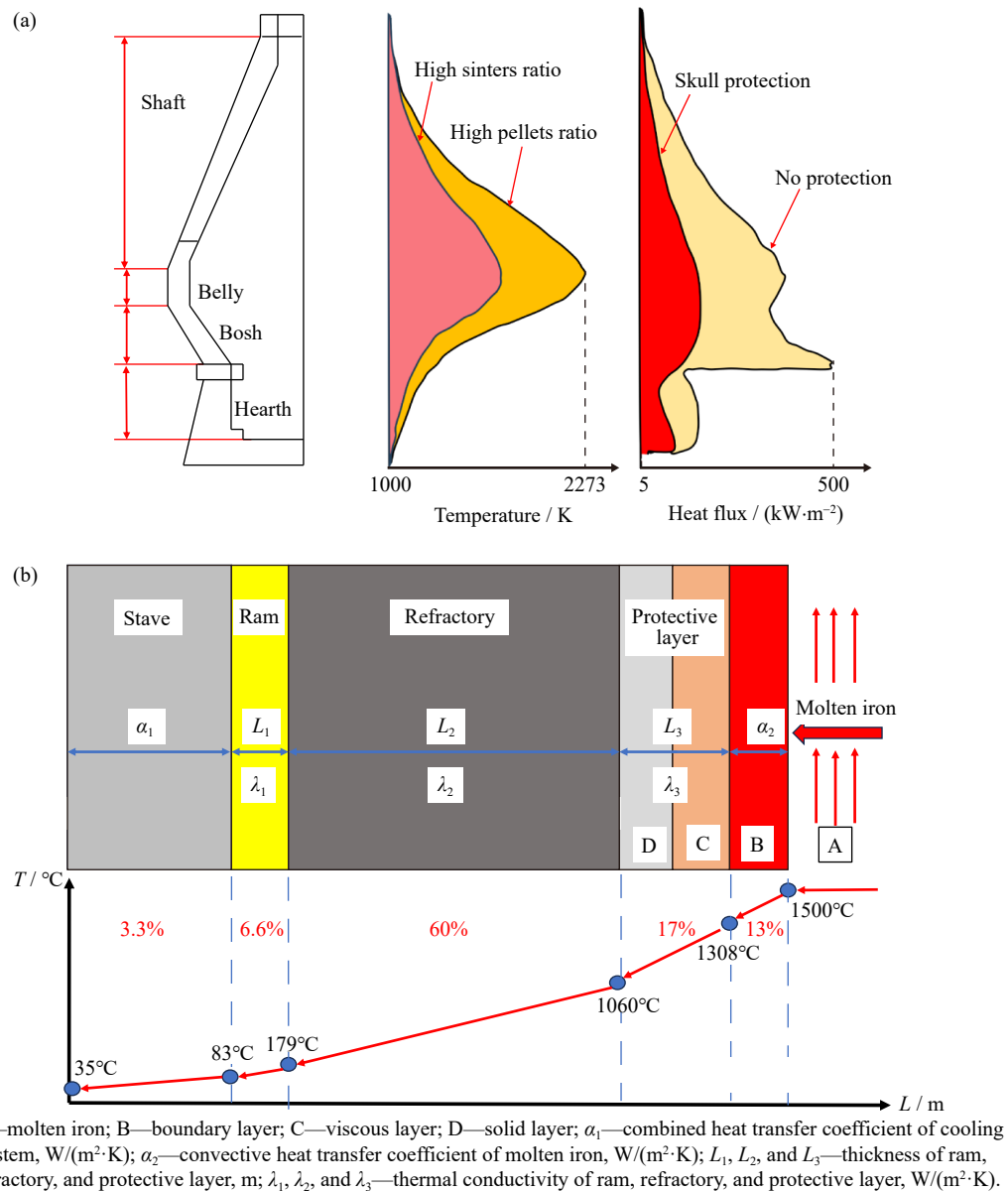
Fig. 3.   (a) Temperature and heat flux distributions in a BF; (b) heat transfer in the hearth (Adapted from Ref. [10]).

employed by establishing 1:1 physical models and mathematical models to simulate water volume distributions under different numbers and angles of inlet pipes around the circumference of BF [19]. Fig. 4 presents the result.

Fig. 4(a) shows the simplified model of the BF cooling system. Plots I, II, and III in Fig. 4(b) reveal the velocity distribution of water when the numbers of inlet pipes are 1, 2, and 3, respectively. With the increase in the number of inlet pipes, although an uneven phenomenon persists, uniformity has increased, and Fig. 4(c) shows thatthe unevenness of water distribution decreases from 46% to 27% as the number of inlet pipes increases from 1 to 3. Fig. 4(d) and (e) shows that the unevenness is negatively correlated with the angle and volume of the inlet pipes. Weak areas within the BF cooling system exhibit a decrease in water flow rate. However, ensuring that minimum velocity exceeds safe water velocity can guarantee BF safety, and a safe water velocity is 1.6 m/s.

[20]. Fig. 4(f) shows the presence of a hidden risk when the water supply volume is small and the weak area is large. As the amount of water increases, the weak areas decrease. When the weak areas cannot be determined, increasing total water volume is a common method for meeting their demand while maintaining safety standards. However, this approach may result in nonweak areas receiving excess water and wasting resources. Precise control can be used to address this issue while promoting uniformity and energy efficiency within the cooling system. The plot IV in Fig. 4(b) presents a simulation diagram that meets the safety requirements of water supply systems, where the method of precisely controlling the valves was used to increase the water velocity in the weak areas while appropriately reducing the amount of water in the nonweak areas, so as to realize uniform water supply, energy saving, and reduction of energy consumption, and achieve the goal of the safety and longevity of the BF.
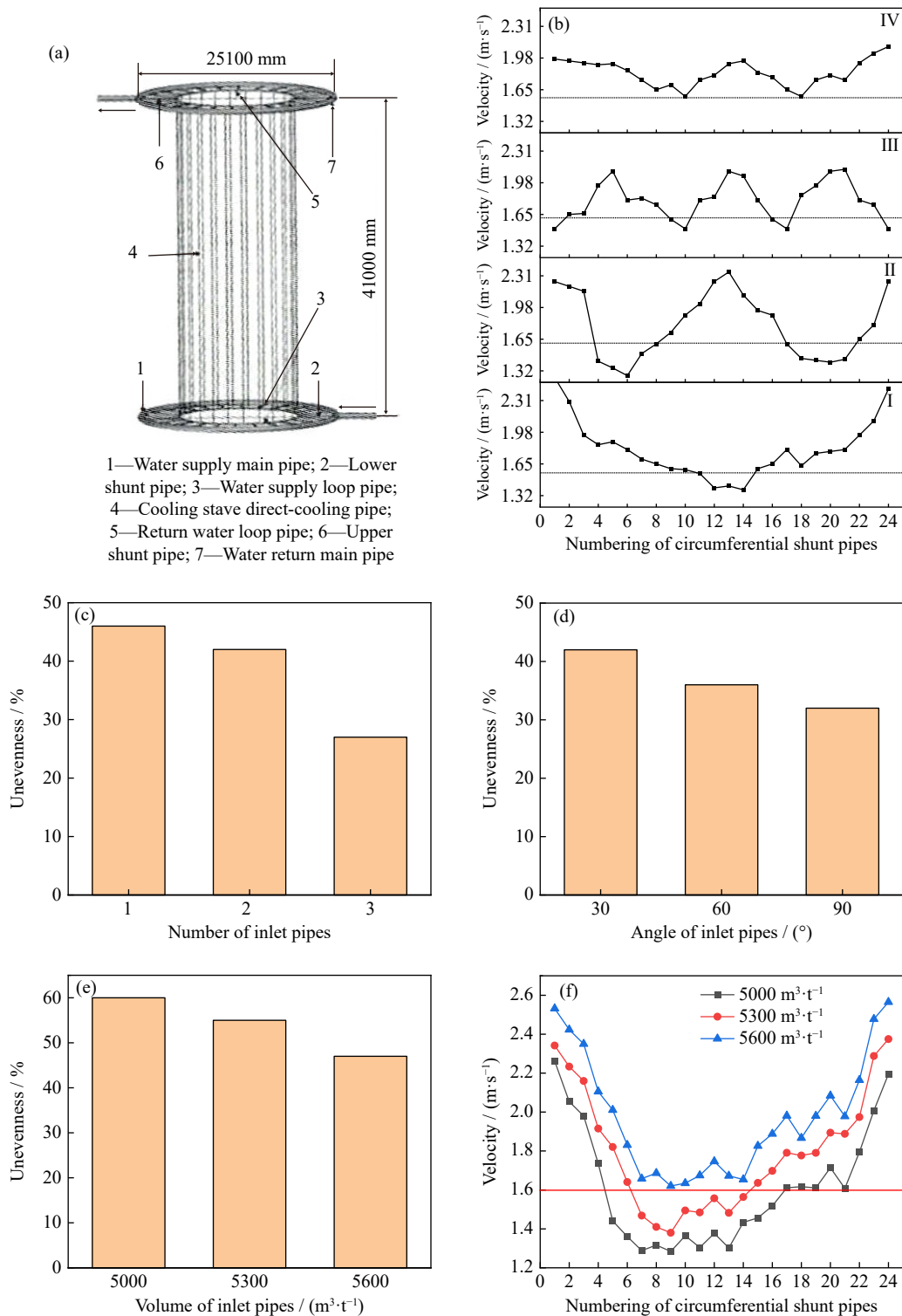
Fig. 4. Uniformity of water distribution in a BF cooling system: (a) the simplified model of the BF cooling system [19]; (b) water velocity distribution; (c) the relationship between the number of inlet pipes and unevenness; (d) the relationship between the angle of inlet pipes and unevenness; (e) the relationship between the volume of inlet pipes and unevenness; (f) variation in velocity with water volume.

2.3. Hydrodynamic characteristics of the BF cooling system

Water pipes within the BF cooling system operate in parallel, which results in fluctuation between individual pipe flows caused by temperature differences. However, the overall circumferential flow remains constant. If temperature differences increase without corresponding decreases in flow rates, redistribution of cooling water under equal amounts must be performed based on the analysis of single-pipe relationship between quantity and temperature difference: large temperature differences correspond to small flows. However, some cooling pipes show consistent water temperature dif-

ferences and water flow rates as a result of the pulsation phenomenon between parallel pipes.

Fluctuations in heat flux within the BF and continuous heating to water in the cooling system result in an instantaneous increase in water temperature. Flow and temperature boundary layers exist near the heating surface of the cooling water pipe, which enables the water within these boundary layers to reach higher temperatures. The elevated temperature of cooling water led to a reduction in dissolved gas solubility and the generation of small bubbles on the pipe wall's heating surface. Gas and bubbles exhibit slower flow rates compared with water, which results in a decrease or cessation of their movement as water flow slows down. Consequently, the flow rate of cooling water through the pipes decreased, and when heat flux intensity increased, corresponding increases in gas and bubble formation occurred. This stage transpired when the evaporation area expanded while water flow decreased. As heat flux declines, gas/bubble quantity decreases, and water velocity increases again. Thus, variations occur in the cooling pipe velocity and temperature difference due to this adaptive phenomenon among parallel pipes within the cooling system. However, this adaptability is weak and exhibits hysteresis for single pipes alone. This phenomenon considerably influences the redistribution of water among parallel pipes while reducing fatigue damage potential for cooling pipes.

3. Types and characteristics of cooling equipment

Various cooling equipment are employed throughout the different sections of a BF for catering to distinct cooling needs (Fig. 5). The upper section of the BF typically utilizes cast iron staves. High-heat load areas, such as the belly, bosh, and lower part of the shaft, commonly employ cast iron, copper, or copper–steel composite staves or copper cooling plates.

3.1. Cast iron stave

The belly and the lower part of the shaft in BF requires the use of several types of cast iron staves, including four-inlet and four-outlet cooling staves, six-inlet and six-outlet cooling staves, double-layer cooling water pipe cooling staves, and inlaid copper-strip cooling staves. Fig. 6 shows the vari-

ous kinds of cast iron staves. Under the same hot surface working conditions and cooling water parameters, the maximum temperatures of the four-inlet and four-outlet cooling stave, six-inlet and six-outlet cooling stave, double-layer cooling water pipe cooling stave, and inlaid copper strip cooling stave reach 450, 370, 350, and 320°C, respectively. This indicated that the double-layered cooling water pipe has a cooling capacity equivalent to that of a six-inlet and six-outlet configuration [21], and inlaid copper-strip cooling staves with higher cooling capacity. In other words, the cooling capacity of the cooling wall is generally characterized by the cooling specific surface area, which is the ratio of the sum of the surface area of the cooling water pipes in the cooling wall to the heated area of the cooling wall, and as the cooling specific surface area increases, the hot surface temperature of the cooling wall decreases.

During the working process, the cast iron cooling stave exhibits high strength and strong resistance to thermal deformation. However, there is a relatively high temperature on the hot surface of the cast cooling stave, due to the air gap between the steel pipe for cooling the water and the cast iron during the casting process and a coating on the surface of the steel pipe, resulting a large thermal resistance and limited heat transfer capacity of cast iron cooling stave [22]. Slag skull formation has become challenging, and the nodular graphite inside these cast iron staves undergoes deformation
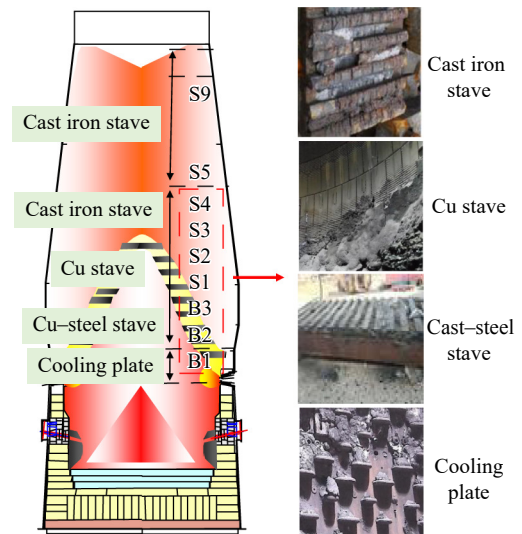

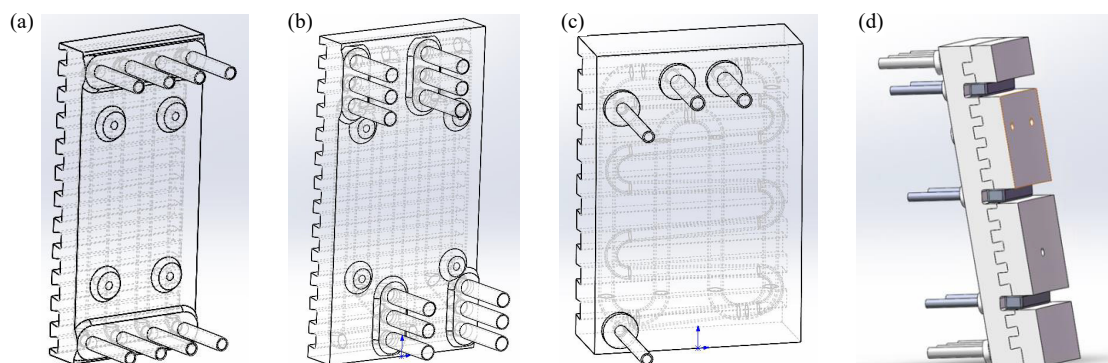**Fig. 5.   Types of staves in different parts of a BF.**

Fig. 6.   Types of cast staves for BFs: (a) four-inlet and four-outlet cooling staves; (b) six-inlet and six-outlet cooling staves; (c) double-layer cooling water pipe cooling staves; (d) inlaid copper-strip cooling staves.

2126

Int. J. Miner. Metall. Mater., Vol. 31, No. 10, Oct. 2024

over prolonged periods (Fig. 7). The cast cooling stave contains a high carbon content (w(C) > 3.0wt%), with carbon existing in the form of spheroidal graphite. Carbon grains grow gradually under high-temperature reactions, which aggravates the formation and expansion of cracks and causes serious cracks, given the already-changed performance of the cast cooling stave. To prolong the campaign of the cast cooling stave, one must determine the evolution law followed by cast iron performance under different temperature conditions and dynamic conditions of change. During the BF operation, the cast cooling stave can form a new protective slag skull within an acceptable period via the control of airflow distribution and slag skull formation, which avoids a sharp change in the performance of the cast cooling stave [23].

3.2. Copper stave

The strong heat transfer capacity, excellent heat flow, and thermal shock resistances of copper stave enable its use in high flux areas of the cooling equipment. Compared with cast iron and cast–steel staves, copper stave has an approximately 9–14 times higher thermal conductivity. The copper stave is drilled to create a cooling water channel, which overcomes the limitations of poor heat transfer performance caused by the presence of high thermal resistance coatings and air gaps in cast iron staves. With its excellent thermal conductivity, the copper stave effectively reduces the temperature on its hot surface, which improves its corrosion resistance for refractory materials that are embedded or sprayed onto it. Over time, during the erosion of refractory materials due to prolonged usage, a slag skull smoothly forms on the hot surface to provide self-protection. However, this slag skull exhibits a relatively low stability and experiences remarkable temperature fluctuations. The large difference in temperature between the copper stave and the slag skull results in substantial thermal stress between these two surfaces. In addition, during slag skull formation, a certain amount of glass phase is present in the slag phase due to the rapid cooling rate. This condition leads to considerable structural stress on the slag skull, which can easily break off under unstable furnace conditions. Consequently, the copper stave experiences frequent temperature fluctuations (Fig. 8(a)). When slags peel off from its surface, the rapid increase in temperature results in considerable thermal shocks and an immediate increase in heat flow intensity. This sudden rise also causes the rapid temperature increase of water within boundary layers, which leads to thermonuclear boiling. This event is followed by film boiling phenomena that further elevate temperatures on the hot surface while degrading the high temperature and anti-wear performances of the copper stave.

With the descent of charge and the flow of gas-carrying dust particles, the copper stave gradually thins over time and may develop leaks. According to statistics, copper stave has an average service life of 6.3 years [25]. Fig. 8(b)–(e) shows the condition of some copper staves after service. Damages to the stave mainly concentrate at the junction of the lower shaft and bosh and the junction of the bosh and belly. Research shows that the wear of large-scale BF copper staves
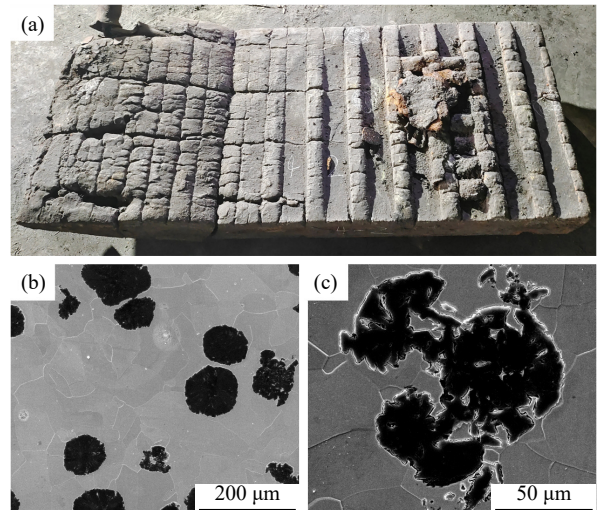
Fig. 7. Changes of the cast cooling stave before and after service: (a) damaged morphology of the cast cooling stave after service, (b) microstructure of the cast cooling stave before sevice, and (c) microscopic morphology of the cast cooling stave after service.

mainly results from charge wear, airflow erosion, and high temperature [26]. As the hearth diameter continues to increase, it becomes difficult for lower airflow to blow through its center while edge airflow easily forms, resulting in slag skull instability. Large-scale BFs bear heavy charger columns, which subject them to greater pressure compared with medium and small BFs. This increased compressive stress exacerbates furnace wear. Prolonging the lifespan of copper staves involves ensuring the stability of slag skull formation and preventing their direct exposure to high-temperature gases and hot descending charges. In addition, hydrogen-related issues associated with cooper-stave under hydrogen-rich smelting conditions require research attention.

3.3. Copper–steel composite cooling stave

The copper–steel composite cooling stave is constructed using oxygen-free copper and steel through explosive welding technology. This technique allows for the bonding of the two materials together. The hot surface of the cooling stave comprises copper, which renders the component with excellent heat transfer capabilities. Conversely, the cold steel surface prevents deformation in high-temperature environments. The combination of these materials allows the copper–steel composite cooling stave to maintain the high thermal conductivity of copper and the strength of steel. The cooling stave has an average tensile strength of 310 MPa, which meets the required strength for practical engineering structures. In addition, the stave has a shear strength of 220 MPa, which can withstand forces applied perpendicularly to its surface [27]. Thus, copper–steel staves can meet the strength requirements of actual engineering structures.

The copper–steel bonding region of the copper–steel composite cooling stave shows an obvious wavy structure, which can be divided into three parts: the interface area between copper and steel, the deformation area between the interface and the area near matrix, and the area near matrix (copper or
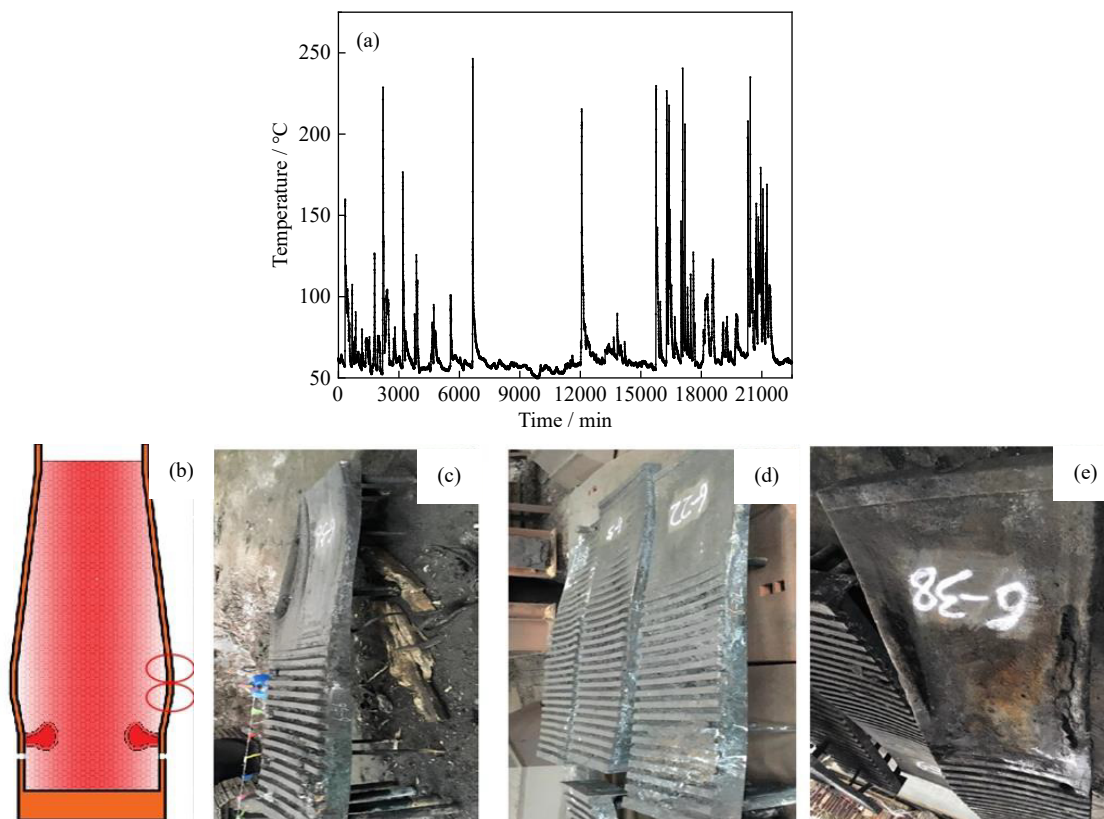
Fig. 8. Stress condition and application characteristics of the copper stave in BFs: (a) temperature change of copper stave in 15 d; (b) damage locations of copper staves; (c) deformation of copper staves; (d) wear of copper stave; (e) damage of copper stave [24].

steel) [27]. Microhardness testing revealed the increased microhardness values at the interface and deformed areas of steel and copper, and such results were due to the combined effect of work hardening and grain refinement near the explosive wave at the copper–steel explosive welded interface [27]. Given the tensile capacity and heat transfer capacity, the copper–steel composite cooling stave performs better than the copper cooling stave.

3.4. Copper cooling plate

In high heat flux areas of BFs, reinforced dense copper cooling plates are also employed for their strong thermal conductivity properties. Fig. 9 shows the temperature field distribution on the copper cooling plate. The plates maintained safe working temperatures between 30–40°C and in the presence of a slag skull. However, when thin or no slag skull was present, temperatures reached up to 375°C at the plate fronts. This temperature is higher than the safe working temperature limits for pure copper materials. The high-temperature area always distributed at the front of the cooling plate. The maximum deformation of 2.73 mm was observed at the hot surface of the copper cooling plate. Graphite refractory bricks with high thermal conductivity can be found between the copper cooling plates and can form slag skulls well. The copper cooling plate can ensure the stability of the slag skull, which exhibits a positive effect on the life extension and safe service of the cooler. The copper cooling plate is easy to operate and shows a strong adaptability to changes in raw materials. The pellet ratio of some BFs in China has reached

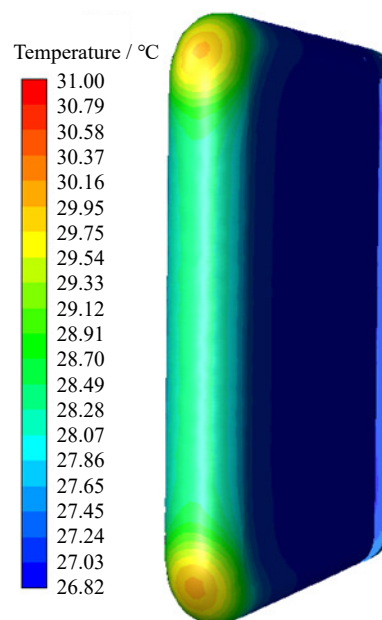more than 30%, and the copper cooling plates of the bosh and belly remain undamaged [28].

Fig. 9. Temperature field distribution of copper cooling plate.

4. Types and characteristics of tuyere sleeve

4.1. Damage characteristics of BF tuyere sleeve

The tuyere sleeve refers to a cooling component with extremely strong heat exchange, which is installed between the hearth and the belly, and it works under the poorest condi-

tions of the BF, as follows: (1) the upper edge of the sleeve is exposed to high-temperature heat radiation of 2000–2200°C and is affected by the removed slag skull or collapsed materials; (2) it experiences slag–iron erosion at approximately 1500°C and microcutting of high-temperature coke; (3) the interior of the tuyere is also influenced by the high-speed hot air at temperatures of 1000–1300°C and the pulverized coal [29–30]. Therefore, the tuyere sleeve is generally made of pure copper, and high-speed water cooling is used to ensure the normal operation of the tuyere sleeve. Under normal circumstances, the service life of the tuyere lasts more than one year. However, several cases revealed that damage and water leakage in tuyere sleeve after a few months or a few days of operation, especially, the front of the tuyere sleeve receives the most damage. Researchers solved this problem by optimizing the tuyere sleeve through improvement of the cooling structure of the tuyere, control of cooling water speed, and addition of a wear-resistant coating. Despite the notable in-

crease in the service life of the tuyere sleeve, some BF tuyere sleeves still fall short of expectations. Damage categories of the tuyere include the following: (1) Dissolution spalling. Potholes of a certain size and irregular shape occupy the front of the damaged tuyere sleeve (Fig. 10), and certain wear and burn marks can be observed. The erosion depth is 18 mm. (2) Burn. Small burning holes are found at the front of the tuyere, and bean-shaped solid iron particles are present inside the holes. The longest diameter of the particles is 9 mm, and the shortest is 3 mm. (3) Abrasion. High-speed movement of coal powder occurs inside the tuyere, which results in wear of the inner wall of the air outlet. The worn tuyere sleeve features a relatively smooth inner surface. (4) Crack. At the front of the tuyere, cracks initiate at the junction of the inner cavity. According to the statistics, the main damage type of tuyere sleeve is dissolution spalling (71.05%), followed by burn (17.25%) and other categories (11.70%) [31–33].

Fig. 10.   Four main damage categories of tuyere sleeve.

4.2. Causes of tuyere sleeve damage in BFs

Fig. 11(a) depicts the microscopic morphology of the erosion damage area of the tuyere sleeve, including a clear three-layer boundary. A sandwich layered structure forms, with the uppermost part serving as the slag–iron area, the middle part as the coexistence area for copper–iron alloy and slag phase, and the lower part as the copper area. The energy dispersive spectroscopy (EDS) result shows (Fig. 11(b)) that the first layer mainly comprises Ca, Si, Mg, and Fe and contains copper and iron particles of different diameters. The second layer is the mixed area of broken copper and

slag–iron. Iron and copper form the copper–iron alloy. A combination of factors, such as high-temperature slag–iron and external impact, causes tuyere sleeve damage. If the slag–iron temperature exceeds the melting temperature of copper, the droplets of copper would formate and diffuse into the slag–iron when high temperature slag–iron contacts with copper tuyere sleeve, and finally form a copper–iron alloy near the interface of slag and iron. Despite the good plasticity and hardness of the copper–iron alloy, the copper side softens with the increase in temperature. Under stress and external forces, iron and copper–iron alloy tend to break and
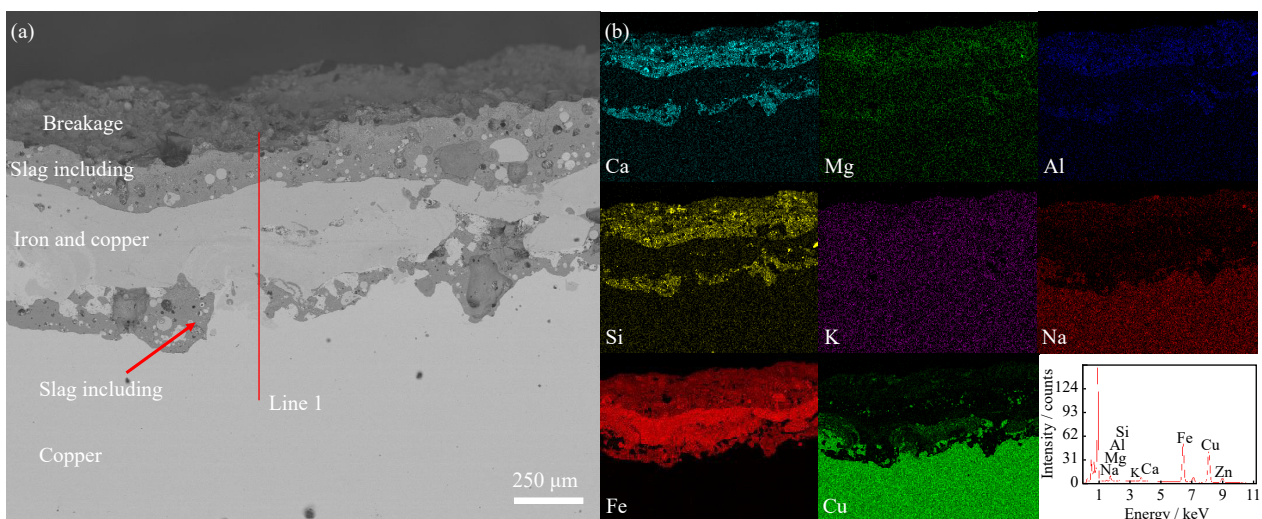

Fig. 11.   Tuyere damage category and damage structure: (a) scanning electron microscopy of the damaged tuyere; (b) EDS of the damaged tuyere [29].

fall off from the copper root. Under repeated actions of the above forces, the melting damage of the copper tuyere sleeve gradually increases and eventually results in water leakage [34].

4.3. New type of tuyere sleeve

Under severe working conditions, the tuyere must have high thermal conductivity, resistance to slag–iron corrosion, and wear resistance. For the prolonged life service and improved thermal conductivity and wear resistance of the tuyere, a wear-resistant layer is applied to the front of the tuyere. For the wear-resistant layer at the front of the tuyere, the commonly used welding methods mainly include metal inert gas welding, laser cladding, and plasma cladding, which use arc, laser, and plasma arc as heat sources, respectively. As a result, the matrix and alloy powder can melt simultaneously under inert gas. One or more metallurgical wear-resisting layers form on the substrate surface [29].

A new type of tuyere sleeve adopts an optimized ring protective layer that cannot only take advantage of the high thermal conductivity of copper but also has an improved wear capability (Fig. 12) [30]. This increases the area of the low-temperature zone at the front of the tuyere sleeve, which will help in the coagulation and stabilization of the slag skull. With the increase in the number of wear-resistant layers, their maximum temperature at the front gradually drops, and the hot surface of the tuyere is likely to form a slag skull. The slag skull is a natural protective layer that can protect itself and reduce the damage caused by contact between high-temperature slag–iron and copper.

5. Performance evaluation of refractory materials for BF hearth

5.1. Characteristics of BF hearth refractory

The safety and longevity of a BF are largely determined by its hearth. Refractory selection is important for the safety and longevity of the hearth. Current hearth refractories mainly include carbon and ceramic bricks with carbon and alumina as the matrix, respectively, and carbon composite brick with an appropriate ratio of carbon and alumina.
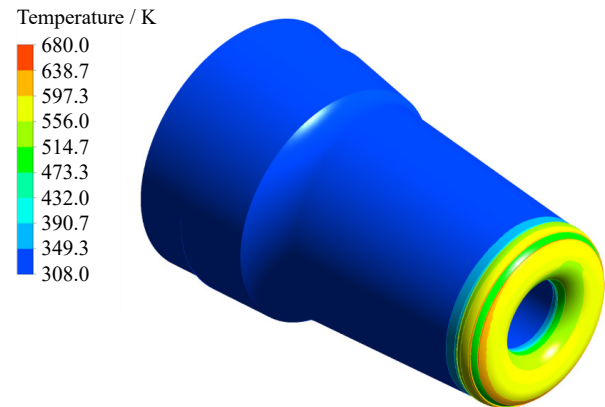

Fig. 12. **Distribution of the temperature field of the tuyere sleeve with ring protective layer [11].**

Table 1 shows the comparison of the performance indexes of different refractories [35–36].

The development of carbon bricks has experienced technological changes several times. The early stage was focused on the microporosity and thermal conductivity of carbon bricks [37]. Furthermore, the focus gradually turned to the optimization of the anticorrosion performance of carbon bricks [38]. The corrosion resistance of molten iron can be improved via two main methods. The first method involves promoting the formation of networked SiC through the addition of elemental Si and reducing the penetration of molten iron of refractory by decrease its pore size. The second method is adding high melting point substances, such as Al_2O_3, TiC, and TiN, to increase the melting point of refractory.

The main raw materials of microporous ceramic brick include corundum and mullite, and the microporosity of the brick makes it highly resistant to molten iron erosion. Therefore, most of researches are focused on the large volume expansion rate of ceramic brick, which is related to the reserved expansion joints during hearth masonry. Insufficient reservation of expansion joints or unreasonable settings causes structural deformation, brick dislocation, and accidents, such as collapse and floating of the ceramic cup. In addition, if the reserved gap is extremely large and the carbon and corundum bricks cannot fit well, harmful elements may penetrate and erode the carbon brick. Therefore, the design of

Table 1. **Comparison of performance indexes of refractory materials for BF hearth [35–36]**

Brick category	Apparent porosity / %	Anticorrosion of molten iron / %	Average pore size / μm	Volume ratio of pore <1 μm / %	Thermal conductivity at 600°C / (W·m⁻¹·K⁻¹)	Compressive strength / MPa	Anticorrosion of molten slag / %	Volume expansion / %
Carbon brick 1	15.45	29.56	0.18	79.90	13.47	53.54		
Carbon brick 2	17.00	13.46	0.11	78.67	14.00	29.41		
Carbon brick 3	10.02	31.17	0.08	88.20	18.15	31.95		
Carbon brick 4	15.05	19.42	0.12	76.08	18.67	44.25		
Ceramic brick 1	10.08	0.79	0.12	87.17	3.61	207.29	4.89	1.64
Ceramic brick 2	10.00	0.91	0.16	78.19	5.42	66.08	23.08	5.84
Ceramic brick 3	11.59	0.82	13.0	14.66	4.34	102.75	100.00	12.44
Ceramic brick 4	12.07	0.88	3.50	9.18	4.63	121.92	100.00	9.57
Carbon composite brick	10.96	0.31	0.24	80.44	14.27	74.09	2.80	2.15

the furnace lining should consider the volume expansion of the brick.

Carbon composite brick refers to a new type of BF refractory material, which introduces appropriate carbon components into the alumina to composite ceramic and carbon materials. This brick type has the dual advantages of carbon and ceramic bricks. The composite brick contains considerably more carbon than ordinary ceramic bricks. The increase in internal carbon contact of composite brick results in a thermal conductivity close to that of the carbon brick. In addition, composite brick has a notably better oxidation resistance than carbon bricks as the alumina provides barrier protection and possesses excellent resistance to molten iron erosion, slag erosion, and alkali metal invasion [39–41].

5.2. Evolution mechanism of refractory microcrack propagation

The corrosion degree of refractories affects the sensitivity of hearth refractories to thermal shock damage [42–43]. Destruction of refractory materials often occurs in the heating and cooling process as changes in temperature cause stress inside the refractory materials. Within the elastic range, stress is proportional to the elastic modulus and elastic strain of the refractory. The elastic strain is equal to the product of the coefficient of linear expansion and change in temperature. Therefore, temperature stress can be expressed as follows:

$$\sigma = E\alpha\Delta T / (1-\mu) \qquad (1)$$

where σ refers to temperature stress, MPa; α denotes the coefficient of linear expansion, $°C^{-1}$; E represents the effective elastic modulus, MPa; ΔT indicates the temperature difference, $°C$; μ is the transverse shrinkage coefficient (Poisson's ratio).

Cracks occur when temperature stress exceeds the flexural strength of the refractory. Once a crack occurs, it will expand due to stress and continue growing in a uniform stress field until complete failure. Crack generation is the main reason for the structural failure of refractory. On the premise of refractory elastic properties and based on the thermoelastic theory of crack formation, the maximum allowable temperature difference (ΔT_{max}) of the material can be expressed as follows:

$$\Delta T_{max} = [\sigma_f (1-\mu) C] / (E\alpha) \qquad (2)$$

where σ_f refers to the flexural strength (MPa), and C indicates the shape coefficient.

With the same shape factor, according to the thermoelastic theory, under thermal shock conditions, new cracks will occur when the thermal stress of the refractory material exceeds its breaking strength. Table 2 shows the calculation results of the thermal shock resistance of different carbon bricks [44]. When the temperature fluctuation of the carbon brick exceeds 201°C, new cracks will occur, which will result in brick fracture.

Table 2.   Thermal shock resistance of different carbon bricks [44]

Carbon brick	σ / MPa	μ	α / $(10^{-6}·°C^{-1})$	E / GPa	C	ΔT_{max} / °C
NMA	11.0	0.101	4.6	7.68	1	280
9RDN	14.8	0.214	4.3	13.48	1	201

5.3. Service safety evaluation of BF refractories

The refractory material simultaneously experiences multiple effects, such as high temperature and pressure, gas flow erosion, melt erosion, harmful element erosion, and charge wear in the BF (Fig. 13). Therefore, the evaluation to the safety performance of refractories under high temperature is

important [45–46]. The evaluation method, in terms of resistance to molten iron erosion, slag erosion, and harmful element erosion, is described as follows.

(1) Alkali corrosion resistance. The dissection study of the BF hearth and investigation of damage revealed the formation of an annular crack along the circumference of the BF
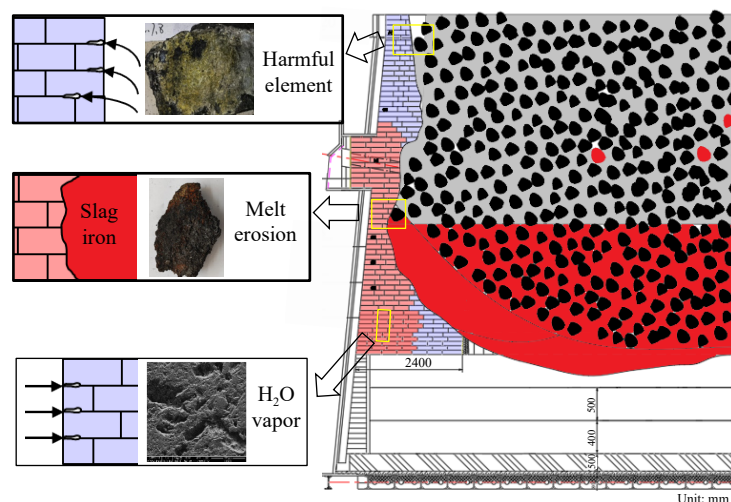

Fig. 13.   Service environment of refractories in the hearth.

hearth on the brick lining [47–48]. The formation of an annular crack on brick lining is divided into two parts. Harmful elements, such as alkali metals, accumulate in the annular seam. The harmful element vapor is assumed to diffuse into the refractory material through open pores and microcracks and then reacts with the ash content of brick lining, which causes volume expansion, during which the compactness of the refractory is destroyed and cracks are formed. With the continuous penetration of harmful element vapors into the cold surface of carbon bricks, vapors eventually condense into liquids at the temperature of 800°C. Afterward, a liquefied element deposits in this area, which causes the erosion of the refractory and eventual formation of ring cracks. Once the ring crack is formed, this area becomes a high thermal resistance area inside the brick lining, which prevents the cooling of the brick lining. This condition seriously threatens the safety and affects the campaign of the BF. Fig. 14 shows the experimental device for refractory resistance to alkali metal corrosion designed for the simulation of actual BF working conditions. The mixed reagent sample is prepared at a certain ratio of K_2CO_3 (Na_2CO_3) and C, thoroughly mixes with an agate mortar, and then places at the bottom of the double-layer graphite crucible. The sample is placed on the graphite gasket, and the graphite crucible is sealed. The crucible is heated up to a temperature of 1200°C for 1 h at the rate of 5°C/min and then cooled to 800°C for 3 h. High-purity argon is introduced as a protective gas throughout the experiment. After the test, the sample is removed and cooled to room temperature with argon for further testing.

(2) Resistance to water vapor and oxidation. The water vapor resistance of the refractory can be measured using a self-assembled thermogravimetric device that can accurately measure and control water vapor content (Fig. 15). The heating element is a silicon molybdenum rod, and deionized water is mixed with the carrier gas (air, oxygen, or argon) in a gas mixing tank after passing through a flow-controlled syringe pump (range: 0.001–9.999 mL/min). The gas flow is controlled by a mass flow meter. The tank is placed in a small heating furnace, and the temperature is controlled above 300°C to ensure full vaporization of the liquid deionized water passing through the tank and its even mixing with the carrier gas. The mixed gas enters the high-temperature furnace through a silicone tube wrapped with a heating wire (the temperature is controlled above 100°C) to prevent the water vapor from condensing. The crucible ($w(Al_2O_3) = 99.9\%$, $w(Al_2O_3)$ means Al_2O_3 content in mass) containing the sample is suspended under a precision balance (accuracy: 0.1 mg). During the test, mass change in the sample is measured online using a balance and recorded with a computer program. The experimental atmosphere includes dry air and wet
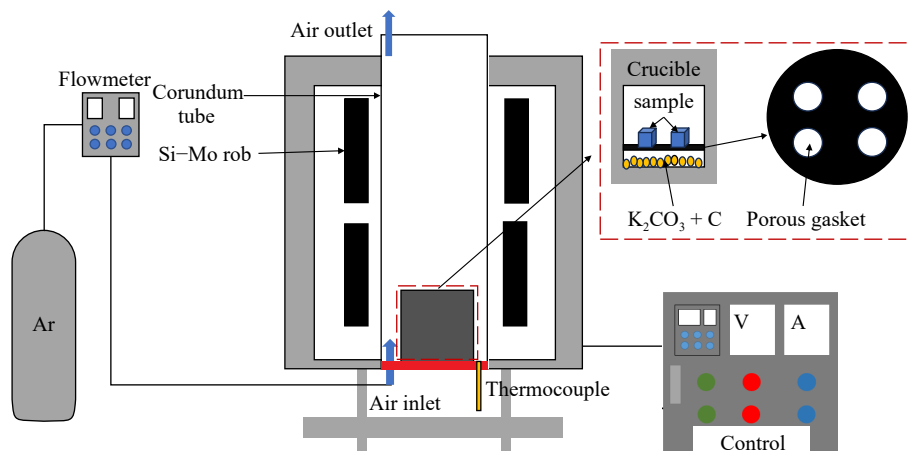

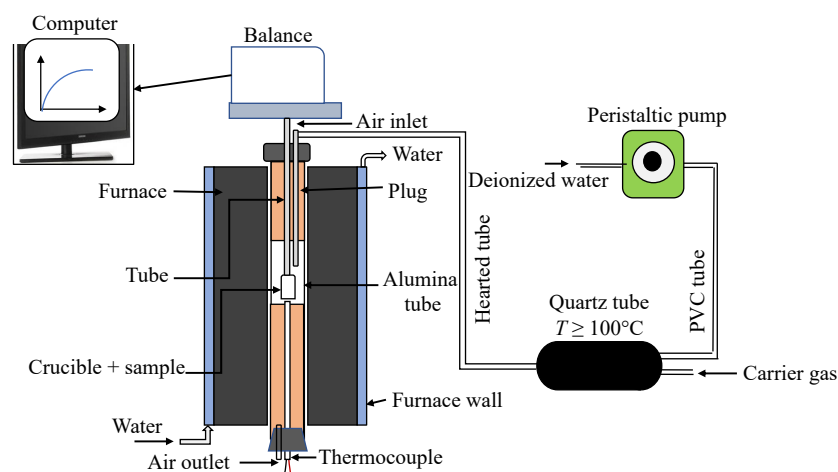**Fig. 14.   Schematic of the alkali erosion experiment device.**

Fig. 15.   Schematic of the water vapor corrosion experiment device. PVC—polyvinyl chloride.

argon with different volume fractions. At the start of the experiment, the heating furnace is heated to 600°C at the heating rate of 5°C/min. The temperature controller of the gas mixing tank and heating wire are heated to 300 and 100°C, respectively. When both reach the specified temperature, water vapor is injected at a rate of 0.06 mL/min, and the carrier gas is released at a rate of 100 mL/min to ensure that the deionized water enters the heating furnace in the form of water vapor. When the temperature of the heating furnace reaches 600°C, the sample is placed in the corundum crucible, which is hung in the constant temperature zone for 10 h. The quality change of the sample is recorded. After the experiment, the sample is retrieved for further testing.

(3) Resistance to slag and iron corrosions. Direct contact with the molten iron will cause the dissolution of [C] in the refractory into molten iron, which results in refractory damage [49–51]. Oxide in the refractory dissolution into the slag will also cause refractory erosion. Most of traditional studies

on slag–iron corrosion resistance of refractories consider the effects of molten iron or slag independently. There are few reports on the erosion process of refractory in combined effect of slag and molten iron. In fact, the erosion of refractory, service in blast furnace, at the interface between slag and molten iron is the most serious, so it is necessary to improve the detection method of the resistance of slag–iron corrosion for refractory. Fig. 16 shows an improved experimental device for slag–iron erosion. The typical BF slag and iron components are selected as experimental reagents. Synthetic slag and iron samples are prepared and placed in a MgO crucible with a graphite crucible above the crucible to ensure safety during the experiment. The furnace is heated to 1550°C, and the sample to be tested is inserted into the crucible. After securing the sample at the center of the crucible, the sample is rotated at a rate of 200 r/min. After the experiment, the sample away is lifted from the flux and cooled with protective gas for the subsequent test.
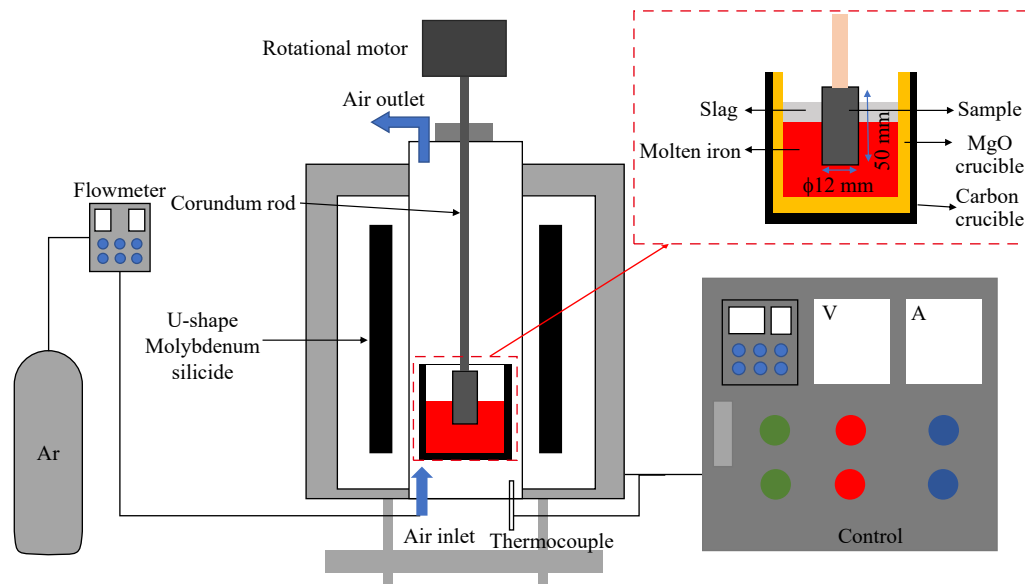

Fig. 16.   Schematic of the experimental device for slag–iron erosion.

6. Technical ideas for the safety and longevity of BF equipment

6.1. BF operation and maintenance technology

Proper operation and maintenance methods must be ensured during the service process of key BF equipment [52–53]. The slag skull should be the core of control in the high-heat flux area. In the BF hearth area, the focus should be allotted to the control of the protective layer. In the discharge of slag and iron, the stability of the liquid level, furnace, slag skull, and protective layer must be ensured. In taphole maintenance, the quality of the taphole clay must be secured, a reasonable taphole depth must be maintained, and the circulation and erosion of molten iron must be reduced.

6.2. BF self-repair technology

The BF self-repair technology promotes the carburization of molten iron via the regulation of the active state of the

hearth and the optimization of the heat transfer system structure of the hearth. Reasonable regulation enables the hot surface of the hearth lining to form a protective layer that isolates the corrosion of slag and iron to the refractory and realizes the self-repair of the BF hearth. According to the analysis of the formation mechanism of the graphite-rich protective layer, from the perspective of phase composition, carbon components of the protective layer mainly originate from molten iron, and graphite can be precipitated only during the saturation of the carbon content in molten iron. In terms of formation conditions, graphite can be precipitated only when the hot-surface temperature of a hearth refractory is lower than the precipitation temperature of graphite [54–55].

6.3. Full-life cycle control technology

Erosion of hearth refractory is a common problem in large-scale BFs. The safety and longevity of BFs can be realized through the establishment of a full-life cycle mainten-

ance concept, the development of different regulation strategies for various service periods, and the strengthening of the supervision and maintenance of BF hearths [56]. First, the design of the hearth and use of high-quality refractory must be optimized to ensure that reasonable furnace lines can be formed at the initial working stage of the furnace. Afterward, the BF operation should be improved to boost productivity in the medium term of the service. Under necessary conditions, the addition of a small amount of titanium-containing material strengthens the protection of the furnace. In addition, the increased amount of Ti in molten iron can stimulate the precipitation of graphite.

7. Research prospects for safe service of key equipment

BFs are the main high-temperature vessels for ironmaking, and they attain the best energy conversion efficiency and will continue to dominate the ironmaking production process. The safety and longevity of BFs are preconditions for low-carbon and high-efficiency ironmaking. The design, operation, maintenance, and monitoring are all critical to the safety and longevity of BFs [57].

The achievement of BFs with safety and longevity requires excellent design, strict construction, proper operation, and scheduled maintenance. The emission peak and carbon neutrality stimulate the rapid development of new technologies and processes of ironmaking. Hydrogen metallurgy and semi- and fully-automatic ironmaking processes have gradually emerged. However, considerable work is still needed to guarantee the safety of key BF materials service and provide precise prevention and control for potential problems.

(1) Carry out basic theoretical research. As equipment materials operate under high temperatures, the evolution law and damage and failure mechanism of large-size equipment materials must be explored under complex and long-time conditions to establish a forecast and prediction system that guarantees the safety of BF equipment. A reasonable design of the BF cooling system is a necessary condition to ensure the long life of BFs. A reasonable cooling system process layout is the key to prevent the overheating of the cooling system in the cooling stave and hearth of BF in the long-term production process and for the formation of a stable protective layer on the hot surface of the cooling stave and hearth. These methods effectively improve ironmaking technology.

(2) Develop new cequipment. BFs have strict requirements for equipment materials and components under high-temperature and high-pressure working conditions. On this basis, scholars should develop a new type of cooler with high thermal conductivity, excellent resistance to slag and iron corrosions and harmful element erosion; the cooler should also have low structural stress tuyeres and small sleeves with low cost and long service life. In addition, the ceramic phase can be creatively added to the carbonaceous composition, and the *in-situ* formation of fibrous SiC whiskers can be reasonably controlled. Carbon–ceramic composite bricks with a high thermal conductivity and excellent melting corrosion resistance can be developed, and safety service evaluation standards for new refractories suitable for the actual working conditions of the BF hearth should be established. These methods can ensure the safety of BFs.

(3) Coordinate BF equipment and design. Self-repair capability is the key to ensuring the safety and long service life of key BF equipment. The self-healing property of the hearth is realized through the regulation of its active state to promote the carburization of molten iron and optimize its heat transfer system to increase the precipitation of graphite carbon from molten iron. Different BFs require various equipment, design, and materials. With safety and long service life as the core objectives, improving the safety and smelting efficiency of BFs should involve the coordination of design, material selection, and routine maintenance.

(4) Construction of BF safety assessment system. Safety has dual characteristics of accuracy and fuzziness. The fusion of multisource heterogeneous data can be used to establish a big data integration monitoring platform for the whole service period while taking advantage of artificial intelligence (AI) algorithms to conduct real-time safety assessments and predictions for key BF equipment. An industrial visualization platform for BF ironmaking will enable the comprehensive monitoring and management of the production process. An application system based on data-driven prediction–internal visualization–intelligent diagnosis and control can be constructed. Based on AI empowerment, an Internet platform for the comprehensive exploration of the common needs of the steel industry can be established. Precise control of potential risks and standardization of the operation process can lead to safe BF production and protect people's lives and the economic benefits of ironmaking.

Acknowledgements

Conflict of Interest

Jianliang Zhang is an editorial board member for this journal and was not involved in the editorial review or the decision to publish this article. All authors state that there is no conflict of interest.

References

[1] Y.B. Zong, Z.Y. Guo, J.L. Zhang, *et al.*, Formation and modification of cinder in tuyere bird's nest area of blast furnace: A review, *Fuel*, 358(2024), art. No. 130236.

[2] J. Perpiñán, M. Bailera, B. Peña, L.M. Romeo, and V. Eveloy, High oxygen and SNG injection in blast furnace ironmaking with power to gas integration and CO_2 recycling, *J. Clean.*

2134

Int. J. Miner. Metall. Mater., Vol. 31, No. 10, Oct. 2024

Prod., 405(2023), art. No. 137001.

[3] X.Y. Zhang, K.X. Jiao, J.L. Zhang, and Z.Y. Guo, A review on low carbon emissions projects of steel industry in the World, *J. Clean. Prod.*, 306(2021), art. No. 127259.

[4] L. Wang, P.M. Guo, L.B. Kong, and P. Zhao, Industrial application prospects and key issues of the pure-hydrogen reduction process, *Int. J. Miner. Metall. Mater.*, 29(2022), No. 10, p. 1922.

[5] C.Y. Xu, *Research on Reduction Behavior of Fluxed Pellets Underhydrogen-Rich Conditions in Blast Furnace* [Dissertation], University of Science and Technology Beijing, Beijing, 2022, p. 20.

[6] Z.J. Hu, Y.M. Chen, and Q.Z. Ju, Baosteel's BF long campaign production practice and exploration, *Ironmaking*, 36(2017), No. 6, p. 1.

[7] X.F. Wang, G.J. Sun, and J.M. Zhu, Long campaign experiences of Baosteel's No.3 blast furnace from corrosion investigation, *Ironmaking*, 35(2016), No. 5, p. 17.

[8] W.X. Wang, Review on development of Chinese ironmaking technology in 2017, [in] *2018 Chinese Ironmaking Production Technology and Iromaking Academic Anual Meeting Proceedings*, Hangzhou, 2018, p. 20.

[9] Z.Y. Xiang, Study of long campaign life technology of blast furnace hearth in foreign countries, *Ironmaking*, 32(2013), No.5, p.53

[10] K.X. Jiao, J.L. Zhang, Z.J. Liu, and T.J. Yang, Analysis of key issues on longevity of blast furnace hearth, *Iron Steel*, 55(2020), No. 8, p.193.

[11] W.T. Zhu, *Research on the Structural Design and Performance Optimization of Low-Carbon Longlife Tuyere for Blast Furnace* [Disseration], University of Science and Technology Beijing, Beijing, 2024, p. 48.

[12] K.X. Jiao, J.L. Zhang, Z.J. Liu, Y. Deng, and C.L. Chen, Cooling phenomena in blast furnace hearth, *J. Iron Steel Res. Int.*, 25(2018), No. 10, p. 1010.

[13] S.B. Kuang, Z.Y. Li, and A.B. Yu, Review on modeling and simulation of blast furnace, *Steel Res. Int.*, 89(2018), No. 1, art. No. 1700071.

[14] B.Y. Guo, D. Maldonado, P. Zulli, and A.B. Yu, CFD modelling of liquid metal flow and heat transfer in blast furnace hearth, *ISIJ Int.*, 48(2008), No. 12, p. 1676.

[15] Y. Kaymak, H. Bartusch, T. Hauck, H. Mernitz, H. Rausch, and R.S. Lin, Multiphysics model of the hearth lining state, *Steel Res. Int.*, 91(2020), No. 11, art. No. 2000055.

[16] Q. Liu and S.S. Cheng, Heat transfer and thermal deformation analyses of a copper stave used in the belly and lower shaft area of a blast furnace, *Int. J. Therm. Sci.*, 100(2016), p. 202.

[17] K.X. Jiao, J.L. Zhang, Z.J. Liu, and H.B. Jiang, Cooling efficiency and cooling intensity of cooling staves in blast furnace hearth, *Metall. Res. Technol.*, 116(2019), No. 4, art. No. 414.

[18] L.J. Wu, W.G. Zhou, H.E. Cheng, Y.L. Su, X.J. Li, and C.Y. Song, The study of cooling channel optimization in blast furnace cast steel stave based on heat transfer analysis, *Int. J. Adv. Manuf. Technol.*, 29(2006), No. 1-2, p. 64.

[19] . L.Y. Hao, K. Wang, and K.X. Jiao, Numerical simulation of homogeneous water supply of BF cooling system, *Ironmaking*, 38(2019), No. 6, p. 24.

[20] K.X. Jiao, J.L. Zhang, G.W. Wang, and C.L. Chen, Investigation of water distribution features among pipes in BF hearth, *Metall. Res. Technol.*, 116(2019), No. 1, art. No. 121.

[21] H. Zhang, K.X. Jiao, J.L. Zhang, and Y.B. Chen, A new method for evaluating cooling capacity of blast furnace cooling stave, *Ironmaking Steelmaking*, 46(2019), No. 7, p. 671.

[22] H. Zhang, K.X. Jiao, J.L. Zhang, and J.P. Liu, Comparisons of the microstructures and micro-mechanical properties of copper/steel explosive-bonded wave interfaces, *Mater. Sci. Eng. A*, 756(2019), p. 430.

[23] H.B. Ma, K.X. Jiao, C. Wang, *et al.*, Investigation of formation and shedding behavior of slag crust in a large blast furnace with copper stave: Flow properties and crystallization characteristics, *J. Sustainable Metall.*, 7(2021), No. 2, p. 506.

[24] T.L. Gao, K.X. Jiao, J.L. Zhang, and Y.B. Zong, Study on non-uniform wear of blast furnace copper stave, *Min. Metall.*, 30(2021), No. suppl. 2, p. 113.

[25] H.B. Ma, K.X. Jiao, J.L. Zhang, L. Zhang, and X.Y. Fan, Phase composition and formation mechanism of slag crust in blast furnace, *ISIJ Int.*, 60(2020), No. 11, p. 2357.

[26] C.P. Yeh, C.K. Ho, and R.J. Yang, Conjugate heat transfer analysis of copper staves and sensor bars in a blast furnace for various refractory lining thickness, *Int. Commun. Heat Mass Transf*, 39(2012), No. 1, p. 58.

[27] H. Zhang, K.X. Jiao, J.L. Zhang, and J.P. Liu, Microstructure and mechanical properties investigations of copper–steel composite fabricated by explosive welding, *Mater. Sci. Eng. A*, 731(2018), p. 278.

[28] S.B. Tang, H.W Li, J.H. Liang, X.M. Zhao, W. Zheng, and W.W. Liu, Production practice of high proportion pellet in no.5 blast furnace of TISCO, *Ironmaking*, 33(2014), p.30.

[29] T.L. Gao, K.X. Jiao, J.L. Zhang, and H.B. Ma, Melting erosion failure mechanism of tuyere in blast furnace, *ISIJ Int.*, 61(2021), No. 1, p. 71.

[30] . B. Kumar Das, Reduction in heat losses through air tuyeres in blast furnaces at DSP, *Mater. Today Proc.*, 66(2022), p. 3944.

[31] J. Zhang, R.D. Wang, R. Hu, *et al.*, Failure mode and mechanism of a blast furnace tuyere, *Eng. Fail. Anal.*, 137(2022), art. No. 106294.

[32] G.S. Li, P.Y. Huang, P. Cheng, *et al.*, Analysis of the failure mechanism of a blast furnace tuyere sleeve with protective coating, *Eng. Fail. Anal.*, 153(2023), art. No. 107537.

[33] J.J. Sun, C.G. Bi, C. Chen, Z.X. Di, H.M. Long, and J.X. Li, Study on wear mechanism at the front end of tuyere small sleeve in blast furnace, *Res. Iron Steel*, 45(2017), No. 4, p.46.

[34] T.L. Gao, K.X. Jiao, H.B. Ma, and J.L. Zhang, Analysis of tuyere failure categories in 5800 m³ blast furnace, *Ironmaking Steelmaking*, 48(2021), No. 5, p. 586.

[35] Z.J. Liu, J.L. Zhang, H.B. Zuo, and T.J. Yang, Recent progress on long service life design of Chinese blast furnace hearth, *ISIJ Int.*, 52(2012), No. 10, p. 1713.

[36] R.S. Shou, *Longevity Technology of Blast Furnace in WISCO*, Metallurgical Industry Press, Beijing, 2009.

[37] H.B. Zuo, C. Wang, J.L. Zhang, Y.A. Zhao, and K.X. Jiao, Application status and important technical indexes of BF hearth refractory, *Iron Steel*, 50(2015), No. 2, p. 1.

[38] J.L. Zhang, Z.Y, Wang, K.X. Jiao, C. Wang, and Y.A. Zhao, Slag erosion resistance and hanging mechanism for the refractory in blast furnace hearth, *Iron Steel*, 50(2015), No. 11, p. 27.

[39] N. Prompt and E. Ouedraogo, High temperature mechanical characterisation of an alumina refractory concrete for blast furnace main trough, *J. Eur. Ceram. Soc.*, 28(2008), No. 15, p. 2859.

[40] Y. Deng, J.L. Zhang, and K.X. Jiao, Dissolution mechanism of carbon brick into molten iron, *ISIJ Int.*, 58(2018), No. 5, p. 815.

[41] K.X. Jiao, J.L. Zhang, Z.J. Liu, Z.Z. Liu, Y. Deng, and X.Y. Fan, Corrosion mechanism of carbon brick in the blast furnace hearth by potassium, *Metall. Res. Technol.*, 115(2018), No. 1, art. No. 109.

[42] Z.Y. Guo, J.L. Zhang, K.X. Jiao, Y.B. Zong, and Z.Y. Wang, Occurrence state and behavior of carbon brick brittle in a large dissected blast furnace hearth, *Steel Res. Int.*, 92(2021), No. 11, art. No. 2100273.

[43] K.X. Jiao, X.Y. Fan, J.L. Zhang, K.D. Wang, and Y.A. Zhao, Corrosion behavior of alumina–carbon composite brick in typical blast furnace slag and iron, *Ceram. Int.*, 44(2018), No. 16, p. 19981.

[44] Z.Y. Wang, *Study on Erosion Behavior of Blast Furnace Hearth Carbon Brick in Molten Iron* [Disseration], University of Science and Technology Beijing, 2022: p. 63.

[45] P. Barral, L.J. Pérez-Pérez, and P. Quintela, Numerical simulation of the transient heat transfer in a blast furnace main trough during its complete campaign cycle, *Int. J. Therm. Sci.*, 173(2022), art. No. 107349.

[46] M. Roche, M. Helle, J. van der Stel, G. Louwerse, J. Storm, and H. Saxén, Drainage model of multi-taphole blast furnaces, *Metall. Mater. Trans. B*, 51(2020), No. 4, p. 1731.

[47] L. Shao and H. Saxén, A simulation study of two-liquid flow in the taphole of the blast furnace, *ISIJ Int.*, 53(2013), No. 6, p. 988.

[48] S. Vázquez-Fernández, A. García-Lengomín Pieiga, C. Lausín-Gónzalez, and P. Quintela, Mathematical modelling and numerical simulation of the heat transfer in a trough of a blast furnace, *Int. J. Therm. Sci.*, 137(2019), p. 365.

[49] X.Y. Fan, K.X. Jiao, J.L. Zhang, R.Q. Cao, R.S. He, and K.D. Wang, Study on physicochemical properties of Al_2O_3–SiC–C castable for blast furnace, *Ceram. Int.*, 45(2019), No. 11, p. 13903.

[50] H. Merten, S. Wirtz, H. Bartusch, *et al*., Analysis of the impact of carbon dissolution and energy transport on the flow in the hearth of an ironmaking blast furnace by transient CFD simulations, *Therm. Sci. Eng. Prog.*, 39(2023), art. No. 101747.

[51] J. Stec, R. Smulski, S. Nagy, K. Szyszkiewicz-Warzecha, J. Tomala, and R. Filipek, Permeability of carbon refractory materials used in a blast furnace hearth, *Ceram. Int.*, 47(2021), No. 12, p. 16538.

[52] F. Bambauer, S. Wirtz, V. Scherer, and H. Bartusch, Transient DEM–CFD simulation of solid and fluid flow in a three dimensional blast furnace model, *Powder Technol.*, 334(2018), p. 53.

[53] K.X. Jiao, C. Wang, J.L. Zhang, S. Ren, and D.Y. E, Heat transfer evolution process in hearth based on blast furnace dissection, *JOM*, 72(2020), No. 5, p. 1935.

[54] K.X. Jiao, J.L. Zhang, Z.J. Liu, F. Liu, and L.S. Liang, Formation mechanism of the graphite-rich protective layer in blast furnace hearths, *Int. J. Miner. Metall. Mater.*, 23(2016), No. 1, p. 16.

[55] S. Meng, K.X. Jiao, J.L. Zhang, *et al*., Dissection study of the deadman in a commercial blast furnace hearth, *Fuel Process. Technol.*, 221(2021), art. No. 106916.

[56] K.X. Jiao, J.L. Zhang, Q.F. Hou, Z.J. Liu, and G.W. Wang, Analysis of the relationship between productivity and hearth wall temperature of a commercial blast furnace and model prediction, *Steel Res. Int.*, 88(2017), No. 9, art. No. 1600475.

[57] F.M. Zhang, Design and operation control for long campaign life of blast furnaces, *J. Iron Steel Res. Int.*, 20(2013), No. 9, p. 53.